AIAA JOURNAL
Vol. 37, No. 11, November 1999

Large Eddy Simulation of Rearward-Facing Step Flow

C. Fureby*
FOA Defence Research Establishment, S-172 90 Stockholm, Sweden

In conventional large eddy simulation (LES) models, the filtered Navier–Stokes equations (NSE) are supplemented by subgrid-scale (SGS) models that emulate the energy transfer from large scales toward the subgrid scales, where it will eventually be dissipated by molecular viscosity. An alternative approach involves solving the unfiltered NSE using high-resolution monotone algorithms for which implicit SGS models are provided by the intrinsic nonlinear high-frequency filters built into the convection discretization. This monotonically integrated LES (MILES) model is to be distinguished from underresolved direct numerical simulation models relying on other numerical methods (not necessarily monotonic) to represent the required damping, which will not necessarily ensure the correct distribution of energy among the large scales. Results from LES and MILES of turbulent rearward-facing step flows suggest that LES is independent of the details of the SGS model if it can adequately channel kinetic energy out of eddies close to the cutoff wave number to prevent aliasing, provided that the resolution is fine enough to ensure that the cutoff wave number is within the inertial subrange. Comparison with experimental data indicates good agreement for global quantities and first- and second-order statistical moments of velocity. Based on the simulations and the comparison with experimental data, the behavior of the flow in the free shear layer and in the reattachment region is presented together with a discussion of flow separation and reattachment.

I. Introduction

SEPARATION and reattachment take place in most high Reynolds number internal and external flow systems, such as diffusors, combustors, and flows around vehicles. In these situations, the flow experiences an adverse pressure gradient, i.e., the pressure increases in the flow direction causing the boundary layer to separate from its confinement. The flow subsequently reattaches downstream forming the recirculation region. In combustor applications, recirculation and turbulence due to separation help enhance mixing of fuel and oxidizer, whereas separation in duct flows causes loss of available energy. Thus, understanding flow separation and reattachment phenomena is important. Among the geometries adopted in studies of separated flows, the most common is the rearward-facing step, due to the morphological and geometrical simplicity and the computational benefits.

The simplest example of a rearward-facing step flow is given by a uniform flow of velocity u_0 in a domain without the upper boundary passing a step of infinite height. This configuration is very close to a free shear layer with zero velocity on one side. Such a flow has, for instance, been studied by Wygnanski and Fiedler,[1] who performed an extensive experimental study of large-scale intermittency. By the use of statistical tools, they demonstrated the existence of large-scale fluctuations, which correspond to shedding of coherent vortices as visualized by Brown and Roshko.[2] Moreover, in this configuration Chandrsuda et al.[3] first proposed the possibility for helical pairing in a shear layer. In a rearward-facing step of finite height h, with an upstream velocity that corresponds to a developing boundary layer, Kelvin–Helmholtz-type vortices are shed in the shear layer behind the step, which subsequently undergo various transformations ultimately leading to a new fully developed state.[4–7] The flow can be separated into the shear layer region including the curved shear layer from the initial boundary layer at separation to the point of reattachment x_R and the relaxation region, from x_R to the point of full recovery. Before curvature effects become large, the growth rates and velocity profile are similar to the half-jet,[4] but as the layer evolves, curvature effects develop, and the mixing layer analogy no longer applies. Also the recirculation length depends on the rates of growth of the shear layer into the recirculation region. In the case of a rearward-facing step with an upper boundary, the upper velocity varies with streamwise distance unlike the half-jet, and, more importantly, the velocity in the recirculation region is not zero.

The Navier–Stokes equations[8] (NSE) give a coarse grained continuum description of the dynamics of a fluid satisfying Newton's equations of motion. Currently, direct numerical simulation (DNS), in which all eddies down to the dissipation scales are properly simulated, is almost impossible due to the large computational effort in resolving all scales of motion. Thus, the necessity for alternative, less computationally expensive but still accurate, methods is apparent. In Reynolds averaged simulation[9] (RAS), all degrees of freedom smaller than the size of the largest energy containing eddies (or wavelets) are averaged over to render equations for variables representing the mean flow. The concept of large eddy simulation[10] (LES) lies between the extremes of DNS and RAS using modified NSE, in which eddies smaller than the typical grid spacing are eliminated from the flow by low-pass filtering, whereas their effects on the resolvable motion is provided by subgrid-scale (SGS) models.[11,12] LES and RAS are similar in that both use modified NSE, the difference in practical terms being the definition of a small scale that in LES is related to the grid spacing and in RAS is related to the integral length scale. An alternative[13] involves solving the NSE by high-resolution monotone methods in which nonlinear high-frequency filters are included, providing that implicit SGS models, and thus explicit SGS models, can be dispensed with.

The purposes of this study are to 1) examine the predictive capabilities of LES for separated flow and study the physics of flow separation and reattachment at moderate Reynolds numbers, 2) examine the alleged resiliency of LES models to the specifics of the SGS model and the associated resolution requirements, and 3) generate a database of first- and second-order statistical moments of the velocity for backward facing step flow at $Re = 16 \times 10^3$, 22×10^3, and 37×10^3 that can be used to examine fluid dynamic processes and to calibrate conventional fluid dynamic models.

II. LES Model

The fluid dynamic model used is the incompressible NSE,[8] i.e., conservation of mass and balance of momentum of a linear viscous fluid. In LES, the dependent variables are arranged into grid scale (GS) and SGS components, i.e., $f = \bar{f} + f'$, where $\bar{f} = G \times f$. The kernel G is any function of $\boldsymbol{x}$ and the filter width $\Delta = \Delta(\boldsymbol{x})$ endowed with the properties

$$\int_D G(\Delta, \boldsymbol{x})\, \mathrm{d}^3\boldsymbol{x} = 1, \qquad \lim_{\Delta \to 0} G(\Delta, \boldsymbol{x}) = \delta(\boldsymbol{x})$$

$$G(\boldsymbol{x}, \Delta) \in C^n(\mathbb{R}^3)$$

Received 28 July 1998; revision received 18 March 1999; accepted for publication 2 April 1999.

*Senior Scientist, Division of Weapons and Protection, Department of Warheads and Propulsion. Member AIAA.

having compact support in a domain D. The LES equations follow from convolving the NSE with G using $[\partial_t, G*]f=0$ and $[\nabla, G*]f=[(\partial G/\partial\Delta)*f]\text{grad}\,\Delta+(Gnf)_{\partial D}$ (n being the normal to ∂D). The lack of commutation results in additional terms in the LES equations. Following Refs. 14 and 15,

$$\text{div}\,\bar{v}=0 \tag{1a}$$

$$\partial_t(\bar{v})+\text{div}(\bar{v}\otimes\bar{v})=-\text{grad}\,\bar{p}+\text{div}(\bar{S}-\boldsymbol{B})+\bar{f}+\mathscr{C}(v) \tag{1b}$$

where v is the velocity, p the pressure, $S=2\nu\boldsymbol{D}$ the viscous stress tensor, ν the physical viscosity, $\boldsymbol{D}=\frac{1}{2}(\text{grad}\,v+\text{grad}\,v^T)$ the rate-of-strain tensor, $\boldsymbol{B}=(\overline{v\otimes v}-\bar{v}\otimes\bar{v})$ the SGS stress tensor, f the specific body force, and $\mathscr{C}$ the commutation error. By following Ref. 14, $\mathscr{C}$ can be compared with $\text{div}\,\boldsymbol{B}$, which suggests that $\mathscr{C}$ can be either neglected or amalgamated into $\text{div}\,\boldsymbol{B}$, which is to be modeled.

To complete the conventional LES model (1) and to provide for interactions between GS and SGS components, closure models for $\boldsymbol{B}$ are required. The SGS stress tensor can be decomposed as $\boldsymbol{B}=\boldsymbol{L}+\boldsymbol{C}+\boldsymbol{R}$, where the Leonard term $\boldsymbol{L}=\overline{\bar{v}\otimes\bar{v}}-\bar{v}\otimes\bar{v}$ represents interactions of resolvable eddies to produce subgrid turbulence, the cross term $\boldsymbol{C}=\overline{\bar{v}\otimes v'}+\overline{v'\otimes\bar{v}}$ represents interactions between resolved and unresolved eddies and may transfer energy in either direction but mainly toward the small-scale eddies, and the Reynolds term $\boldsymbol{R}=\overline{v'\otimes v'}$ represents interactions taking place between small-scale eddies as it produces the necessary energy transfer from large to small scales. Mathematical analysis and physical considerations[14–17] suggest that $\boldsymbol{B}$ is a Grammian tensor, provided that $G=G(|x|,\Delta)$, i.e., $G\in SU(3)$, which implies that $\boldsymbol{B}\in Psym$, where $Psym$ is the set of all positive definite symmetric tensors. Also, $\boldsymbol{B}$ is frame indifferent and, therefore, an isotropic function in its arguments. The realizability conditions follow from the Grammian features of $\boldsymbol{B}$ so that the necessary and sufficient conditions for $\boldsymbol{B}\in Psym$ are $\frac{1}{2}\text{tr}\,\boldsymbol{B}\geq 0$, $\frac{1}{2}[k^2-\|\boldsymbol{B}\|^2]\geq 0$, and $\det\boldsymbol{B}\geq 0$.

The most popular SGS models are based on a gradient hypothesis, in which $\boldsymbol{B}=\frac{2}{3}k\boldsymbol{I}-2\nu_k\bar{\boldsymbol{D}}$, where k and ν_k are the SGS kinetic energy and eddy viscosity, which require additional modeling. Common models include the Smagorinsky model,[12] (SMG) $\nu_k=c_D\Delta^2\|\bar{\boldsymbol{D}}\|$, and a one-equation eddy-viscosity model[12] (OEEVM), where k is obtained from a modeled balance equation,[18] i.e.,

$$\partial_t(k)+\text{div}(k\bar{v})=-\boldsymbol{B}\cdot\bar{\boldsymbol{D}}+\text{div}(\nu_k\,\text{grad}\,k)+\varepsilon$$

$$\nu_k=c_k\Delta\sqrt{k},\qquad \varepsilon=\frac{c_\varepsilon k^{\frac{3}{2}}}{\Delta},\qquad c_k=0.07,\qquad c_\varepsilon=1.05 \tag{2}$$

The model coefficients can be determined from the assumption of isotropy and a $|k|^{-5/3}$ inertial subrange behavior, but this approach is questionable in transient cases and in the wall proximity. This provides the motivation for dynamic models where an attempt is made to evaluate the model coefficients dynamically using a second level of filtering[19] with a filter width of 2Δ. Here we use SMG with $c_D=0.02$ and with dynamic evaluation of c_D along fluid-particle trajectories, as suggested by Meneveau et al.[20] In this Lagrangian dynamic Smagorinsky model (DSMG) $c_D=\frac{1}{2}\ell_{LM}/\ell_{MM}$, the nominator ℓ_{LM} and the denominator ℓ_{MM} are obtained from the following relaxation-transport equations:

$$\partial_t(\ell_{LM})+\text{div}(\ell_{LM}\bar{v})=(1/\tau)(L\cdot M-\ell_{LM})$$

$$\partial_t(\ell_{MM})+\text{div}(\ell_{MM}\bar{v})=(1/\tau)(M\cdot M-\ell_{MM}) \tag{3}$$

where $L=\overline{\bar{v}\otimes\bar{v}}-\bar{\bar{v}}\otimes\bar{\bar{v}}$ is the resolved Leonard stress tensor, $M=\Delta^2(\|\bar{\bar{\boldsymbol{D}}}\|\bar{\bar{\boldsymbol{D}}}-4\|\bar{\boldsymbol{D}}\|\bar{\boldsymbol{D}})$ is the Germano strain tensor, and $\tau=\Delta(\ell_{LM}\ell_{MM})^{-1/8}$ is the relaxation time controling the memory length of the averaging. A Gaussian filter kernel have been used for the second level of filtering.

The LES equations and the SGS model of choice are discretized using an unstructured finite volume method so that $D\cup\partial D\rightarrow T_d$, where T_d is a partition of $D\cup\partial D$ into subvolumes Ω_P, of scale d [usually of $\mathcal{O}(\Delta)$] having centroids at x_P and face-area centroids at x_f, which satisfies $\cup_P(\Omega_P)=D\cup\partial D$ and $\cap_P(\Omega_P)=\emptyset$. By letting

$$f_P=\frac{1}{\delta V}\int_{\Omega_P}f\,dV$$

represent the discrete approximation to the cell averages of f over the P:th cell, the Gauss theorem can be used to obtain the semidiscretized LES equations. These are integrated in time by a multistep method[21] to give the discretized LES equations

$$\sum_f[(\bar{v}\cdot dA)]_f=0 \tag{4a}$$

$$\sum_{k=1}^{m}\left\{\alpha_k(\bar{v})_P^{n+k}+\frac{\beta_k\Delta t}{\delta V_P}\sum_f[(\bar{v}\cdot dA)\bar{v}-(\bar{S}-\boldsymbol{B})\,dA]_f^{n+k}+\beta_k\bar{f}_p^{n+k}\Delta t\right\}=-\beta_k(\text{grad}\,\bar{p})_p^{n+m}\Delta t \tag{4b}$$

where α_k and β_k are parameters of the scheme and Δt is the time step. Let $\tilde{f}_f^C(\bar{v};\mu)$ be an approximation to the convective flux $f_f^C(\bar{v})=[(\bar{v}\cdot dA)\bar{v}]_f$ and $\tilde{f}_f^D(\bar{v};\mu)$ be an approximation to the mixed SGS and viscous flux $f_f^D(\bar{v})=[(\bar{S}-\boldsymbol{B})\,dA]_f$, where $\mu=\mu(P)$ represents a set of points in the neighborhood of P. The functional reconstruction of $\tilde{f}_f^C(\bar{v};\mu)$ and $\tilde{f}_f^D(\bar{v};\mu)$ is executed using linear interpolation across the cell faces f of Ω_P and centred difference approximations of the gradients in $\tilde{f}_f^D(\bar{v};\mu)$, which gives centered second-order accurate representations of all fluxes. To decouple the pressure–velocity system, Eq. (4b) is solved for $\bar{v}_f^{n+m}$, the face interpolate of which is used to derive the flux $(\bar{v}\cdot dA)_f$. Eliminating $\bar{v}_f^{n+m}$ between Eq. (4a) and this expression for $\bar{v}_f^{n+m}$ results in the discrete Poisson equation

$$\sum_f\left\{(a_P^{-1})_f[(\text{grad}\,\bar{p})^{n+m}\cdot dA]_f\right\}=\sum_f\left\{(a_P^{-1})_f\left[\left(\sum_{k=0}^{m}\sum_N(a_N^{n+k}v_N^{n+k})+\sum_{k=0}^{m-1}(b_p^{n+k}v_P^{n+k})\right)\cdot dA\right]_f\right\} \tag{5}$$

A segregated approach[22] is used to solve Eqs. (4b) and (5) leading to a Courant number restriction; a maximum Courant number of 0.2 gives satisfactory stability and temporal accuracy.

An important role in the vorticity dynamics of free shear flows is played by the dynamics of slender tubelike regions of vorticity.[23–25] When such regions are much thinner than the main flow scales, the main features are contained in the strengths and positions of the centerlines of such vortices. In such regimes we can expect that models that will handle vortices in a manner similar to that of shocks will provide a good computational framework.[26,27] Similar arguments form the basis of monotone integrated LES[13,28] (MILES) in which the NSE are solved using high-resolution monotone methods with embedded nonlinear filters providing implicit closure models so that explicit SGS models can be dispensed with. Hence, the discretized MILES equations are

$$\sum_f[(v\cdot dA)]_f=0 \tag{6a}$$

$$\sum_{k=1}^{m}\left\{\alpha_k(v)_P^{n+k}+\frac{\beta_k\Delta t}{\delta V_P}\sum_f[(v\cdot dA)v-S\,dA]_f^{n+k}+\beta_k f_p^{n+k}\Delta t\right\}=-\beta_k(\text{grad}\,p)_p^{n+m}\Delta t \tag{6b}$$

The functional reconstruction of $\tilde{f}_f^C(v;\mu)$ is performed using a flux-limiting method, which attempts to hybridize a high-order convective flux function $\tilde{f}_f^H(v;\mu)$ that is well behaved in smooth regions with a low-order dispersion-free convective flux function $\tilde{f}_f^L(v;\mu)$ by using a nonlinear flux limiter Γ. More precisely, $\tilde{f}_f^C(v;\mu)=\tilde{f}_f^H(v;\mu)-(1-\Gamma)[\tilde{f}_f^H(v;\mu)-\tilde{f}_f^L(v;\mu)]$, so that if v is smooth near v_P then Γ should be near unity, although in the vicinity of a discontinuity we require Γ to be near zero. In MILES the

Table 1 Overview of simulations, grids, and global quantities

Case/run	Re, $\times 10^4$	SGS model	Grid; resolution	λ/h	$\partial\delta_\omega/\partial x_1$	$Sr, x_1/h=1$	$Sr, x_1/h=6$	$\Xi, x_1/h=3$
A1	1.5	OEEVM	87,104; 2Δ	6.8	0.25	0.20	0.07	0.13
A2	1.5	OEEVM	204,460; $3\Delta/2$	6.6	0.26	0.19	0.07	0.10
B1	2.2	OEEVM	366,750; $3\Delta/2$	7.1	0.27	0.23	0.06	0.11
B2	2.2	OEEVM	170,400; 2Δ	7.1	0.25	0.23	0.06	0.16
B3	2.2	SMG	170,400; 2Δ	7.2	0.24	0.22	0.07	0.17
B4	2.2	DSMG	170,400; 2Δ	7.1	0.27	0.24	0.07	0.17
B5	2.2	MILES	170,400; 2Δ	7.4	0.25	0.23	0.05	0.15
B6	2.2	OEEVM	1,152,600; Δ	7.0	0.28	0.23	0.06	0.06
C1	3.7	OEEVM	366,750; 2Δ	6.9	0.26	0.25	0.06	0.17
Exp,[31]	1.5	—	—	6.5	0.28	—	—	—
Exp,[31]	2.2	—	—	7.0	0.28	—	—	—
Exp,[31]	3.7	—	—	6.8	0.28	—	—	—

concept of flux corrected transport[29] is used, which attempts to incorporate as much as possible of the correction (or antidiffusion) term $[\tilde{f}_f^H(v;\mu)-\tilde{f}_f^L(v;\mu)]$ without violating the physical principles of causality, positivity, and monotonicity. Here, $\tilde{f}_f^H(v;\mu)$ is based on linear interpolation, whereas $\tilde{f}_f^L(v;\mu)$ is based on first-order upwinding. The flux limiter adopted here is

$$\Gamma = \tfrac{1}{2}[(1-\vartheta/\zeta)\,\mathrm{sgn}(\vartheta-\zeta)+(\vartheta/\zeta)\,\mathrm{sgn}\,\vartheta-\mathrm{sgn}(\vartheta-1)]$$

where ϑ is the normalized variable corresponding to $\frac{1}{2}|v|^2$ and the parameter ζ is assigned a value of 0.1. Note that if $\zeta > 0.5$ the limiter enforces a total variation diminishing conservative scheme. The functional reconstruction of $\tilde{f}_f^D(v;\mu)$, the handling of the pressure–velocity coupling, and the solution method are the same as for the conventional LES model.

With the intent of comparing LES and MILES the modified equations, corresponding to Eqs. (4b) and (6b), involving Taylor series expansions of the discretized equations, can be used. For LES,

$$\partial_t(\bar{v})+\mathrm{div}(\bar{v}\otimes\bar{v}) = -\mathrm{grad}\,\bar{p}+\mathrm{div}(\bar{S}-\boldsymbol{B})+\bar{f}+\tau_t(\bar{v}) + \tau_c(\bar{v})+\tau_d(\bar{v})+\mathcal{O}(\Delta t^3,|\boldsymbol{d}|^3) \tag{7}$$

where $\tau_t(\bar{v})=\frac{1}{3}\Delta t^2\partial_t^3(\bar{v})$ is the leading-order truncation error from a Crank–Nicholson time integration and

$$\tau_c(\bar{v}) = \mathrm{div}([\boldsymbol{G}\,\mathrm{grad}\times(\mathrm{grad}\,\bar{v})]_{\mathrm{sym}})$$

is the leading-order truncation error from to the linear interpolation used in the functional reconstruction of $\tilde{f}_f^C[\bar{v};\mu(P)]$, whereas $\tau_d(\bar{v})$ is of $\mathcal{O}(|\boldsymbol{d}|^2)$, the exact expression depending on the SGS model applied. Similarly for the MILES model,

$$\partial_t(v)+\mathrm{div}(v\otimes v) = -\mathrm{grad}\,p+\mathrm{div}\,S+f+\tau_t(v) + \mathrm{div}(v\otimes r+r\otimes v+r\otimes r)+\tau_c(v)+\tau_d(v)+\mathcal{O}(\Delta t^3,|\boldsymbol{d}|^3) \tag{8}$$

where $\tau_t(v)$, $\tau_c(v)$, and $\tau_d(v)$ are similar to the leading-order truncation errors of the conventional LES model and where $\mathrm{div}(v\otimes r+r\otimes v+r\otimes r)=\mathrm{div}\,\boldsymbol{B}=-(\boldsymbol{C}\boldsymbol{L}^T+\boldsymbol{L}\boldsymbol{C}^T+\beta^2\boldsymbol{L}\boldsymbol{d}\otimes\boldsymbol{L}\boldsymbol{d})$, with $r=\beta(\mathrm{grad}\,v)\boldsymbol{d}$, $\boldsymbol{C}=\beta(v\otimes\boldsymbol{d})$, and $\beta=(1-\Gamma)\,\mathrm{sgn}\,v$, is the leading-order truncation error that may be interpreted as the implicit or builtin SGS model. $\boldsymbol{B}$ may be decomposed into $\boldsymbol{B}^{(1)}=-(\boldsymbol{C}\boldsymbol{L}^T+\boldsymbol{L}\boldsymbol{C}^T)$ and $\boldsymbol{B}^{(2)}=-\beta^2\boldsymbol{L}\boldsymbol{d}\otimes\boldsymbol{L}\boldsymbol{d}$ of which the former is a generalized eddy-viscosity model with $\boldsymbol{C}$ being a second-rank eddy-viscosity tensor and the latter is of a form essentially similar to the scale-similarity models. Borue and Orszag[30] recently studied some statistical properties of the SGS stress tensor, the energy flux, and the velocity gradients and concluded that a term of the form $\boldsymbol{B}^{(2)}$ improved the correlations between the exact and modeled SGS stress tensor. This form also permits the eigenvectors of $\boldsymbol{B}$ to be different from those of $\boldsymbol{D}$, possibly alleviating some of the limitations of the eddy-viscosity models.

III. Description of the Rearward-Facing Step Flow Problem and the Simulations

The problem under consideration is the rearward-facing step of Pitz and Daily[31] consisting of a channel followed by a smooth contraction to one-half of its height continued by the step expansion into the test section (Fig. 1). In this study three cases, characterized by different inlet velocities u_0 and labeled by the step-height Reynolds number $Re=u_0h/\nu$, are examined using LES and MILES models on different grids. Results from these simulations are compared with experimental data[31] and with RAS results. In particular, we show results from the standard k–ε model on two-dimensional versions of a coarse LES grid using the same numerical methods as for LES. RAS using more advanced turbulence models, such as nonlinear k–ε models and differential stress models, have been carried out and will be the subject of a future investigation. Four grids, with different numbers of grid points, are used; they all share the same topology and are concentrated to the shear layer region and near both channel walls while geometrically stretched in other regions.

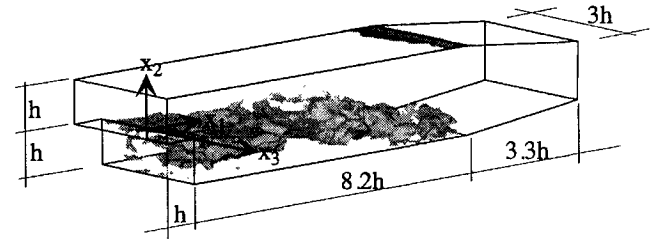

Fig. 1 Perspective view of the configuration,[31] with coordinate system attached to the corner of the step at the centerplane; also an isosurface of the instantaneous longitudinal velocity component, i.e., $\bar{v}_1$, separating backward and forward flow regions.

All simulations start from rest, and the unsteady flow characteristics evolves naturally. At the inlet $\mathrm{grad}\,\bar{p}\cdot\boldsymbol{e}_1=0$ and $\bar{v}=\bar{u}(x_2)\boldsymbol{e}_1+\boldsymbol{u}'$, where $\bar{u}(x_2)$ is the experimentally measured profile, $\boldsymbol{e}_i$ is a unit-vector in the x_i direction, and $\boldsymbol{u}'$ represents a random white noise perturbation on the order of 4, 2, and 2% in the streamwise, spanwise, and normal directions, respectively. Although the application of white noise is a poor representation of turbulence, it has proved adequate for this case, with the results found to be insensitive to the level of the prescribed fluctuations. At the outlet boundary a Dirichlet condition is used for $\bar{p}$, whereas $\bar{v}$ is subjected to a zero Neumann condition. In the spanwise direction, periodic conditions are enforced, and for the upper and lower channel walls, no-slip conditions for $\bar{v}$ and zero Neumann conditions for $\bar{p}$ are adopted. Table 1 presents an overview of the simulations, the grids, and the values of some key parameters such as the recirculation length λ, the mean vorticity thickness $\delta_w=(\bar{v}_1^u-\bar{v}_1^l)/(\partial\bar{v}_1/\partial x_2)|_{\max}$, where $\bar{v}_1^u$ and $\bar{v}_1^l$ are the velocities in the upper and lower streams, and the Strouhal number $Sr=fh/u_0$, at $x_1/h=1$ and 6.

IV. Results: Statistical Comparisons

First- and second-order statistical moments of $\bar{v}$ are averaged over the spanwise direction and time. Statistical data are sampled at each time step, starting after the passage of initial transients, i.e., after about three to seven flow-through times, depending on Reynolds number, SGS model, and initial conditions. Simulations using different SGS models are started in sequence and have short initial transient passage times, whereas simulations at different Reynolds numbers, initiated from previous runs by rescaling the velocity according

a) Streamwise $\bar{v}$ component

b) Vertical $\bar{v}$ component

c) Spanwise v' component

Fig. 2 Instantaneous velocity and velocity fluctuation contours in the centerplane.

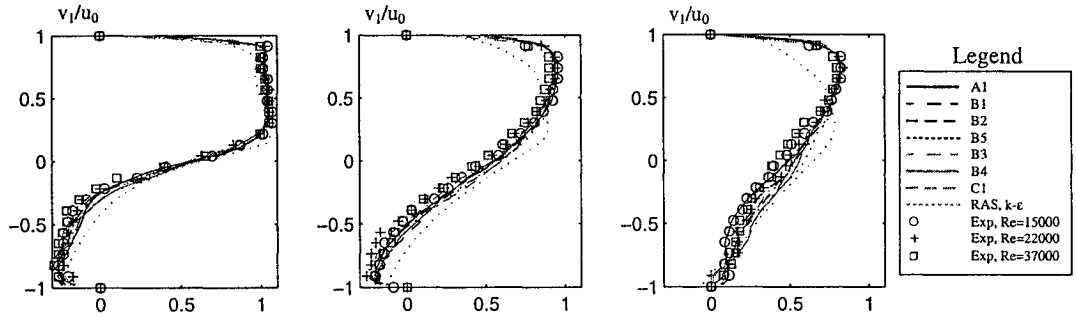

Fig. 3 Streamwise mean velocity profiles $\langle\bar{v}\rangle_1$ downstream of the step at $Re = 15 \times 10^3$, 22×10^3, and 37×10^3 at a) $x_1/h = 2$, b) $x_1/h = 5$, and c) $x_1/h = 7$.

to the Reynolds number ratios, have longer initial transient passage times. The flow-through time is defined as the convection time through the postexpansion region of $11.5h$ at an average convective speed of $0.8u_0$. The necessity of long initial transient times is due to the long residence time in the recirculation region. The final statistical data, collected over an additional 7.8, 7.3, and 7.4 flow-through times depending on Reynolds number, were studied to determine the convergence of turbulence statistics. The convergence is monitored using the relative magnitude of the time-averaged LES equation residues. The statistical variables sampled comprise the mean velocity $\langle\bar{v}\rangle$, the Reynolds stress tensor $\boldsymbol{T} = \langle v' \otimes v'\rangle$, and the rms-velocity fluctuations $v_{\text{rms}} = \text{diag}\sqrt{\boldsymbol{T}}$, where $v' = v - \langle\bar{v}\rangle$ is the velocity fluctuation. In addition, $\bar{p}$ and $\bar{v}$ histories are sampled at 10 points in the centerplane.

Contours of $\bar{v}$ and v' components from run B1 are presented in Fig. 2. The $\bar{v}_1$ distribution in Fig. 2a shows a shear layer emerging from the step and reaching the lower wall at $x_1/h \approx 7$. The $\bar{v}_2$ distribution in Fig. 2b reveals vertical flow patches, concentrated to within the shear layer and inside the recirculation bubble. The flow is mostly downward downstream of the reattachment line, although alternating positive and negative $\bar{v}_2$ regions are found which indicate spanwise Kelvin–Helmholtz vortices. High gradients are found in all velocity components within the shear layer and near reattachment. Maximum $\bar{v}_1$ occurs in the free shear layer just downstream of reattachment, and $\bar{v}_2$ reaches its minimum value at reattachment, where the downward fluid impinges on the lower wall. Figure 2c shows contours of v^3_{rms} having peak values reaching as high as $0.5u_0$ near reattachment. Although it seems that maximum values of v^i_{rms} are of $\mathcal{O}(0.1u_0)$ in the recirculation region, the low streamwise velocity causes the fluctuations to reach as high as 40% of $\bar{v}_1$. The near-wall region appears laminarlike in the simulations as well as in experiments,[31,32] which suggests that the reverse flow is laminarlike but with the unsteadiness imposed by the turbulent shear layer.

The importance of spatial resolution has been investigated for the $Re = 22 \times 10^3$ case, using the OEEVM model. For this purpose three grids are chosen so that the ratios of the characteristic grid spacings, $\Delta = (70h^3/N^3)^{1/3}$, where the nominator represents the computational volume, are approximately 2Δ, $3\Delta/2$, and Δ for runs B2, B1, and B6, respectively. Results from comparison of statistical data (Figs. 3 and 4) signify that $\langle\bar{v}_1\rangle$, v^1_{rms}, and v^2_{rms} are reasonably well predicted on the intermediate grid with only small errors on the coarse grid. In particular we study the ratio of SGS kinetic energy to resolvable energy, i.e., $\Xi = \langle k\rangle / \frac{1}{2}\langle|\bar{v}|^2\rangle$. Table 1 presents cross sectionally averaged values of Ξ at $x_1/h = 3$, which may serve as illustrative examples of how the distribution of Ξ changes with spatial resolution. It is evident that Ξ, and thus k, decreases with increasing spatial resolution and that k carries about 6% of $\frac{1}{2}\langle\bar{v}^2\rangle$ for the Δ grid and about 16% of $\frac{1}{2}\langle\bar{v}^2\rangle$ for the 2Δ grid, which indicate that the resolution is marginal for LES. However, recent studies by Woodruff et al.[33] suggests that LES may predict first- and second-order statistical moments satisfactorily even at coarse grids provided that the model parameters are properly adjusted. This supports the findings in the present study concerning spatial resolution and grid dependence. The grids used for cases A1, A2, and C1 are obtained by conjecturing that the cutoff wave number falls within the inertial subrange, so that the total number of grid points scale according to $N^3 = \mathcal{O}(Re^{3/2})$.

Figure 3 presents a compact comparison of $\langle\bar{v}\rangle_1$ between LES using OEEVM, SMG, and DSMG models, MILES, and experimental data[31] for cases A1, B1, B2, B3, B4, B5, and C1 (cf. Table 1). Comparison is made at three locations: two in the recirculation region

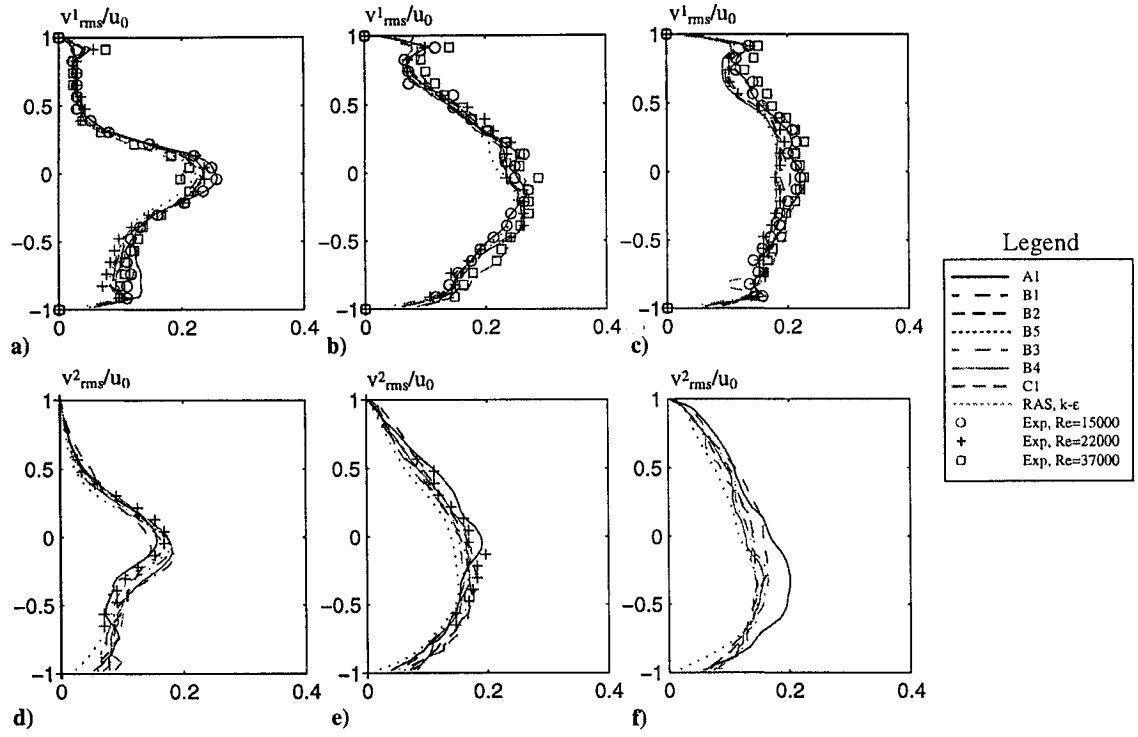

Fig. 4 Streamwise (v^1_{rms}) and vertical (v^2_{rms}) rms-velocity fluctuations at $Re = 15 \times 10^3$, 22×10^3, and 37×10^3 at a) $x_1/h = 2$, v^1_{rms}; b) $x_1/h = 5$, v^1_{rms}; c) $x_1/h = 7$, v^1_{rms}; d) $x_1/h = 2$, v^1_{rms}; e) $x_1/h = 5$, v^2_{rms}; and f) $x_1/h = 7$, v^2_{rms}.

$x_1/h < \lambda/h$ and one in the recovery region, i.e., between the closure of the recirculation bubble and $x_1/h \approx 8$, where the flow accelerates despite the adverse pressure gradient it faces. Because all data are nondimensionalized with h and u_0, both measured and calculated profiles are expected to collapse onto a single profile. For the low Reynolds number, i.e., case A1, good agreement with measurement data is found, although the maximum reverse velocity is slightly underpredicted, i.e., $0.30u_0$ as compared to the experimental value of $0.33u_0$. Grid refinement (case A2), using a characteristic resolution of $3\Delta/2$ instead of 2Δ, gave a maximum reverse velocity of $0.31u_0$. Eaton and Johnston[4] report reverse velocities of $0.25u_0$, and the higher value observed here and in the experiments may be due to the low aspect ratio or the influence of the upper wall. For the medium Reynolds number case (cases B1–B6) similar conclusions can be drawn for the grids examined. The $\langle\bar{v}\rangle_1$ component appears grid independent, and the SGS models tested produced very similar results; details of these simulations will be further discussed later. The simulations slightly underpredict the maximum reverse velocity, between $0.30u_0$ and $0.32u_0$, as compared to the experimental data of $0.33u_0$. A k–ε simulation[9] was carried out for this Reynolds number on a two-dimensional version of the 2Δ grid. The results are overlaid in Fig. 3, and from this comparison it is evident that even coarse grid LES outperforms the k–ε model. For the high-Reynolds-number case, i.e., case C1, similar observations can be made.

The reattachment location x_R is determined from the location of the mean dividing streamline and gives reattachment lengths λ according to Table 1. These are all in very good agreement with the experimental values but somewhat overpredicted. From the average streamlines of the mean flow, a secondary recirculation region is found in the step corner, extending to between $1.2h$ and $1.0h$ in the x_1 direction depending on the Reynolds number and to about $0.7h$ in the x_2 direction, which seems to agree quantitatively with experimental results[34] giving a value of $\lambda/h = 0.9$ but at $Re = 1.13 \times 10^5$. From other studies, λ is known to be sensitive to the expansion ratio, Reynolds number, inlet turbulence, and initial boundary-layer thickness, and here we find λ almost constant in $15 \times 10^3 < Re < 37 \times 10^3$. By changing the magnitude of the perturbations at the inlet by 50%, we found no significant changes in the flow topology, first- and second-order statistics, or in the reattachment length.

In Fig. 4, profiles of v^1_{rms} and v^2_{rms} are presented for cases A1, B1, B2, B3, B4, B5, and C1 together with the experimental data at the locations used in Fig. 3. Regions of intense turbulence are confined by the shear layer and spread as the layer widens downstream. Near reattachment, the turbulence decreases, and the rms-profiles begin to take on the characteristics of channel flow. The positions of the maximum values initially coincide with the centerline but dip toward the recirculation region and rise toward the centerline near reattachment, which concurs with the measurements presented.[4,31] The peak values of v^1_{rms} and v^2_{rms} increase at first, due to the formation of large coherent structures, to finally stabilize around 22 and 16% of u_0, respectively, correlating well with measurement data.[31] From Fig. 4, we note that the distributions of v^1_{rms} and v^2_{rms} are in good qualitative and quantitative agreement with the experimental results, although the predicted profiles are not as smooth as could be expected. This can be compensated for by sampling data for longer periods of time. The general tendency is that the agreement between predictions and experiments for v_{rms} declines with distance from the step and can be explained by the reduction of resolution in streamwise direction as the grid is stretched, thus filtering out larger and more energetic structures. Hence, v_{rms} appear more sensitive to the spatial resolution than $\langle\bar{v}\rangle$.

Large-scale temporal oscillations are observed from animating the flow; even from the contour plots of Fig. 2 it is anticipated that the free shear layer has a vertical motion causing the reattachment location to oscillate. Temporal fast Fourier transform analysis has been applied to the time histories of the velocity components sampled at some points along $x_3 = 0$ during an interval of $50h/u_0$. The power density spectra of the fluctuating component kinetic energies are shown in Fig. 5 as function of the nondimensional frequency or the Strouhal number $Sr = fh/\bar{v}_1$. Spectra are presented at two locations downstream of the step for run B1 (Figs. 5a and 5b), for different Reynolds numbers (Fig. 5c) and for different SGS models (Fig. 5d). All spectra exhibit a well-defined $Sr^{-5/3}$ range over one decade. From Figs. 5a and 5b, the energy in the smaller scales are found more evenly distributed among the velocity components, indicating a trend toward isotropy. The distribution of the energy in the larger scales is anisotropic, the $\bar{v}_1$ component being the most energetic. Figure 5c suggests that the dominating frequencies are in $0.06 < Sr < 0.08$, with Strouhal numbers corresponding

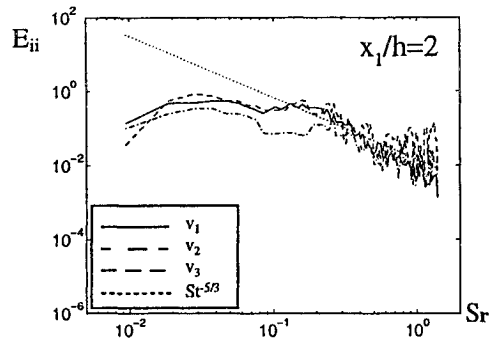

a) Component-based spectra for case B2 at $x_1/h = 2$

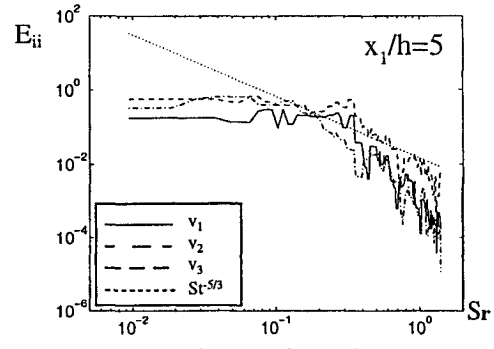

b) Component-based spectra for case B2 at $x_1/h = 5$

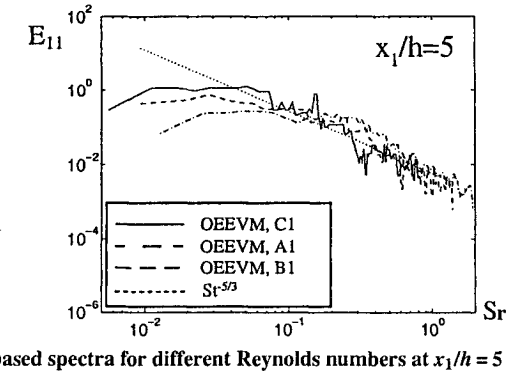

c) $\bar{v}_1$-based spectra for different Reynolds numbers at $x_1/h = 5$

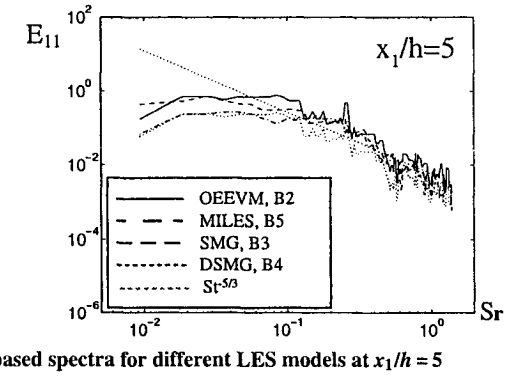

d) $\bar{v}_1$-based spectra for different LES models at $x_1/h = 5$

Fig. 5 Energy spectra downstream of the step.

to $Re = 15 \times 10^3$, and higher to $Re = 37 \times 10^3$, which is further corroborated by experiments.[31,33]

V. Results: SGS Model Performance

In this section results from LES at $Re = 22 \times 10^3$, using OEEVM, SMG, DSMG, and MILES will be examined. The simulations will be referred to as runs B3, B2, B4, and B5, respectively, according to Table 1 and are performed on the 2Δ grid to enhance potential differences. Visual examination of the $\langle \bar{v}_1 \rangle$, v^1_{rms}, and v^2_{rms} fields (cf. Fig. 2) give no advice to which LES model performs best because they give almost identical predictions of the large-scale dynamics. The power density spectra of the fluctuating component kinetic energies, $\frac{1}{2}\bar{v}_i^2$, all exhibit a well-defined $Sr^{-5/3}$ range over one decade, and the peaks of the $\bar{v}_1$-component kinetic energies are in $0.07 < Sr < 0.08$. In addition, the mean reattachment lengths are all within 7% of the experimental data (see Table 1).

Figures 3 and 4 present typical profiles of $\langle \bar{v} \rangle_1$, v^1_{rms}, and v^2_{rms} and provide comparisons with the experimental data. All LES models give similar profiles, and the agreement between simulations and experiments is very good. The mean streamwise velocity from the OEEVM was already found independent of spatial resolution, and hence, the other SGS models are expected to show the same behavior. To examine this, LES on a grid similar to that of B6 were performed for DSMG, SMG, and MILES, for which statistics were compiled over a limited period of time, i.e., $25h/u_0$. Results from SMG and DSMG gave similar reattachment lengths, i.e., $\lambda = 7.1h$, whereas for MILES some improvements were found: λ dropped from $7.4h$ to $7.2h$, which is close to the experimental value of $7.0h$ but still higher than the results from OEEVM. For both rms fluctuations, v^1_{rms} and v^2_{rms}, only insignificant differences between the different SGS models can be observed; all LES models show good qualitative and quantitative agreement with measurements, and it is hard to distinguish between model predictions, giving support to other studies[23,28] and references therein that report resiliency of first- and second-order statistical moments to the choice of SGS model.

Probability density functions (PDFs) of the $\bar{v}_1$ components from B2–B5 are shown in Fig. 6. The probability density $\wp$ is defined by

$$\frac{1}{u_0}\int \wp \, \mathrm{d}\bar{v} = 1$$

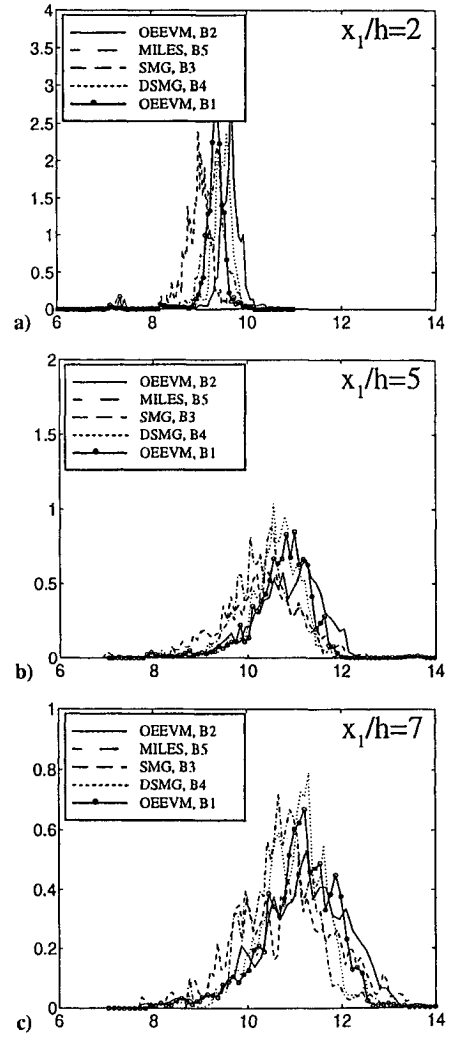

Fig. 6 PDF of $\bar{v}_1$ at locations downstream of the step for different SGS models.

and is constructed from the velocity histories sampled during the last $50h/u_0$ time units in the points $(x_1/h, x_2/h) = (2, 0)$, $(5, 0)$, and $(7, 0)$. Based on the skewness and flatness factors, i.e. the third- and fourth-order statistical moments of the PDFs, the PDFs are classified. The PDFs are known to characterize the details of the flow (cf. Ref. 35), and so we use the PDFs to characterize the LES models. At $x_1/h = 2$ (Fig. 6a) all PDFs have a skewness close to 0 and a flatness of around 3; at $x_1/h = 5$ (Fig. 6b) the skewness is about -0.2 and the flatness is around 3; and at $x_1/h = 7$ (Fig. 6c) the skewness is about 0.1 and the flatness is around 3. At $x_1/h = 2$ the distribution is Gaussian, at $x_1/h = 5$ the distribution is negatively skewed with tails on the low-velocity side, and at $x_1/h = 7$ the distribution is positively skewed with tails on the high-velocity side. When comparing the predicted PDFs with measured PDFs, e.g., Refs. 31 and 35, the qualitative agreement is obvious, which accentuates the general notion that LES is suitable for unsteady separating flows and that the flowfield obtained from LES is a direct consequence of the physical processes described by the filtered NSE and only weakly affected by the SGS flow physics. Comparing PDFs corroborates the conjecture that the results are only weakly affected by resolution. The choice of SGS model is, however, observed to affect the shape of the PDFs: the OEEVM results in PDFs biased toward the high-velocity side, whereas MILES results in rather wide PDFs. Both observations may be related to the ν_k distribution representing the subgrid energy transport and, thus, implicitly affecting all wave numbers close to the cutoff wave number.

To gain further insight into the LES modeling, in Fig. 7 we compare PDFs of the vorticity magnitude $|\bar{\omega}|$ for OEEVM, SMG, DSMG, and MILES models with corresponding PDFs in 512^3 DNS (Ref. 24) and 64^3 LES (Ref. 23) of homogeneous isotropic turbulence. The vorticity, $\bar{\omega} = \frac{1}{2}\text{curl}\,\bar{v}$, is evaluated in subvolumes of the size $h \times h \times h$ centered around $(x_1, x_2, x_3) = (7h, h, 0)$. For the subvolume, $|\bar{\omega}|$ is scaled with its rms value $|\bar{\omega}|_{\text{rms}}$, which is based on velocity data over the time interval of $9h/u_0$. A main difference between these data and data from homogeneous isotropic turbulence relates to the behavior of the PDFs of $|\bar{\omega}|$ for small values because the conditions of the subvolume involve mainly irrotational fluid; probabilities of small values of $|\bar{\omega}|$, for example $|\bar{\omega}| < 0.3$, appear largest when based on the backward-facing step data, whereas smaller probabilities are found when based on analysis of the homogenous turbulence data. For large values of $|\bar{\omega}|$, for example, $|\bar{\omega}| \geq 0.3$, the PDFs based on the backward-facing step and the homogeneous turbulence have similar, monotonically decreasing trends, including the range $0.3 < |\bar{\omega}| < 2.0$, where the slopes of the PDFs appear independent of Reynolds number and tends to coincide. Figure 7 shows similar PDFs of $|\bar{\omega}|$ for all LES models, which also agree reasonably well with the PDF of the homogeneous turbulence; thus, LES appears largely unaffected by the specifics of the SGS models. Moreover, most of the flow is occupied by a relatively weak vorticity with intense vorticity regions, which correspond to vortical structures intermittently passing any position in the flow and representing a small fraction of the volume.

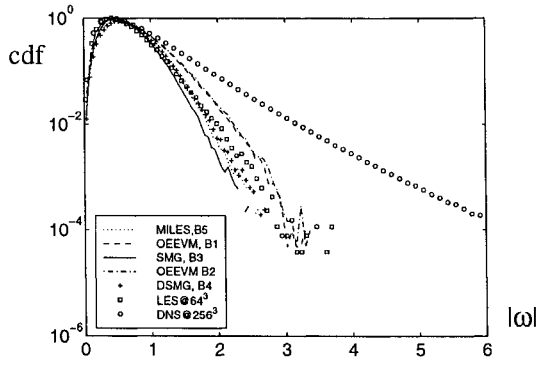

Fig. 7 PDF of the vorticity magnitude $|\bar{\omega}|$ in subvolumes of size h^3 centered around $(x_1, x_2) = (7h, h)$ for OEEVM, SMG, DSMG, and MILES with corresponding PDFs from 512^3 DNS (Ref. 24) at $Re_T = 168$ and 64^3 LES (Ref. 23) at $Re_T = 305$.

VI. Results: Flow Separation and Reattachment

Figure 2 indicates that the shear layer broadens downstream and finally impinges on the lower wall at $x_1/h \approx 7$. It is inclined toward the x_1 axis upstream of the reattachment line and separates the separation bubble from the inflow, which quickly loses its attributes (Fig. 1). Before curvature effects become large, the growth rate and velocity profiles are similar to the half-jet,[4] but due to the upper wall, a characteristic of this case, $\bar{v}_1$ varies with x_1 and t. As the shear layer continues to grow, curvature effects become large, and the analogy to a mixing layer no longer applies. As already observed, $\bar{v}_2$ shows high values in the shear layer and is rapidly attenuated close to reattachment (Fig. 2b). This is primarily due to the impermeability condition at the lower wall, which effectively distorts the large eddies by a mainly inviscid mechanism. The maximum values of the velocity gradients $\bar{L} = \text{grad}\,\bar{v}$ occur in the shear layer, which experiences the most intense strain $\|\bar{D}\|$ and vortex stretching $\bar{\omega} \cdot \bar{L}\bar{\omega}$. Contours of v_3' in Fig. 2c show structures inclined toward the x_1 axis in the shear layer, but become distorted and tilted in the reattachment region. Note that the contours of v_3' correspond to the contours of the actual spanwise velocity because there is no mean flow in the x_3 direction. In contrast to $\bar{v}_1$, here $\bar{v}_2$ and v_3' are organized in smaller structures within the reattachment region. Also, the shear layer fluctuates up and down with a well-defined frequency, characterized by the Strouhal number, to splash fluid toward the lower wall near the mean reattachment line.

Figure 8 presents isocontours of $\bar{\omega}_3$ and $\bar{\omega}_1$, at the centerplane and at a typical x_2–x_3 plane for runs A2, B1, B2, and C1. The shear layer separating from the step rolls up into coherent $\bar{\omega}_3$ vortices due to the shear layer instability. The $\bar{\omega}_3$ vortices have a typical radius of $\mathcal{O}(h)$ but are in turn made up of several $\bar{\omega}_3$ vortices having a typicall radius down to $\mathcal{O}(\Delta)$, i.e., the lower limit is determined by grid resolution. The $\bar{\omega}_3$ vortices undergo helical pairing as they are advected downstream to endure vortex stretching effects due to the three dimensionality of the flow. Once the $\bar{\omega}_3$ vortices have completed their initial rollup, a secondary instability causes the formation of coherent $\bar{\omega}_1$ vortices. These counterrotating vortices usually form in the braid region between adjacent $\bar{\omega}_3$ vortices and are highly coherent rodlike structures, as evident from Figs. 8e–8h. The secondary instability effects appear similar to results obtained by DNS of temporal mixing layers at low Reynolds number (cf. Ref. 36). Farther downstream, vortex stretching breaks down the coherent $\bar{\omega}_3$ vortices whereas the $\bar{\omega}_1$ vortices maintain their coherence and their structure, all the way to the exit of the computational domain. Thus, a key feature of this flow is a transformation of a vorticity distribution initially dominated by Kelvin–Helmholtz, or $\bar{\omega}_3$, vortices into a distribution dominated by $\bar{\omega}_1$ vortices, and it is then important to examine this transition.

Visualizations of $\bar{\omega}$ by means of isosurfaces of $\bar{\omega}_i$ or $|\bar{\omega}|$, as in Fig. 9a, is difficult due to the complexity of the vorticity. Alternatively, low-pressure regions may be used because they almost coincide with the centers of the vortices, but more recently other methods, such as the discriminant method[37] and the Q criterion[38] have been proposed as more appropriate measures of vortical flow regions. For the purpose of examining the transformation from $\bar{\omega}_3$ to $\bar{\omega}_1$ in a backward-facing step flow, the Q criterion, in which regions of $|\bar{\omega}|$ with $|\bar{\omega}|^2 > \|\bar{D}\|^2$ define the regions where rotation is predominant, is considered more appropriate. By following Hunt et al.,[38] let the scalar $Q = \frac{1}{2}(|\bar{\omega}|^2 - \|\bar{D}\|^2)$ be an appropriate measure, then $Q > 0$ represents the regions where rotation is predominant, i.e., the vortex cores. Visualizations of $|\bar{\omega}|$ when filtered by the Q-criterion are presented in Figs. 9b and 9c for runs A2 and B1, respectively. Thus, independent of Reynolds number, the backward-facing step flow transforms spanwise vortical structures into streamwise vortical structures. In the first $2h$ downstream of the step, the flow consists predominantly of spanwise vortical structures, which are gradually transformed during the next $4.5h$ into streamwise vortical structures that characterize the flow in the remaining part of the computational domain. Based on visualizations of the Q-criterion (Figs. 9b and 9c) a possible scenario for the vortex dynamics in a rearward-facing step flow can be that quasi-two-dimensional Kelvin–Helmholz vortices are shed of the step. Between $2h$ and $4h$ these undergo helical-pairing interactions and,

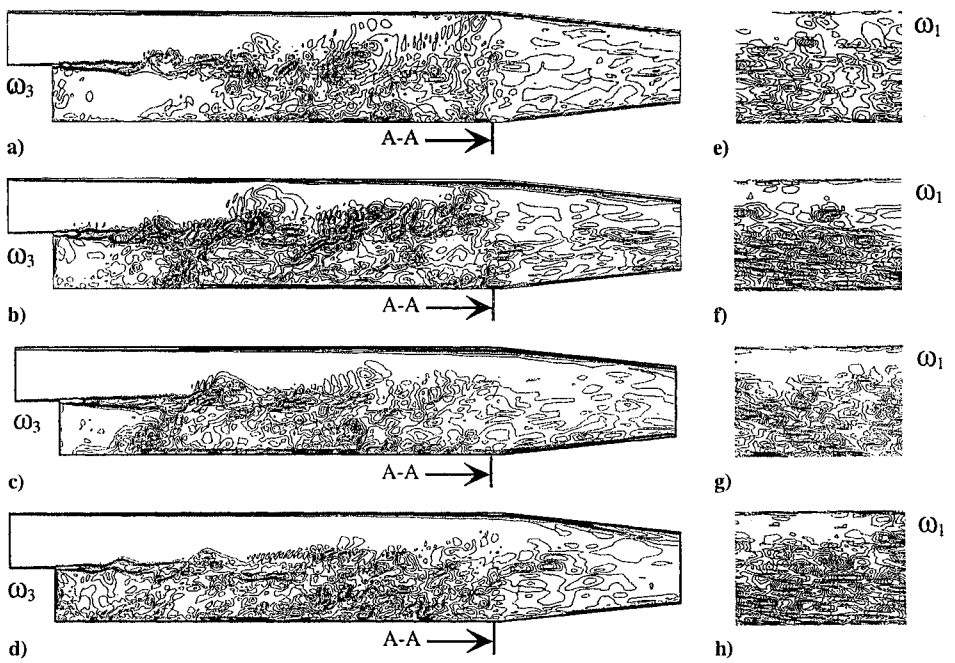

Fig. 8 Instantaneous spanwise $\bar{\omega}_3$ and streamwise vorticity $\bar{\omega}_1$ contours normalized with the step height and inflow velocity in typical x_1–x_2 and x_2–x_3 planes: a) $\bar{\omega}_3$ run A2, b) $\bar{\omega}_3$ run B1, c) $\bar{\omega}_3$ run B2, d) $\bar{\omega}_3$ run C1, e) $\bar{\omega}_1$ run A2, f) $\bar{\omega}_1$ run B1, g) $\bar{\omega}_1$ run B2, and h) $\bar{\omega}_1$ run C1.

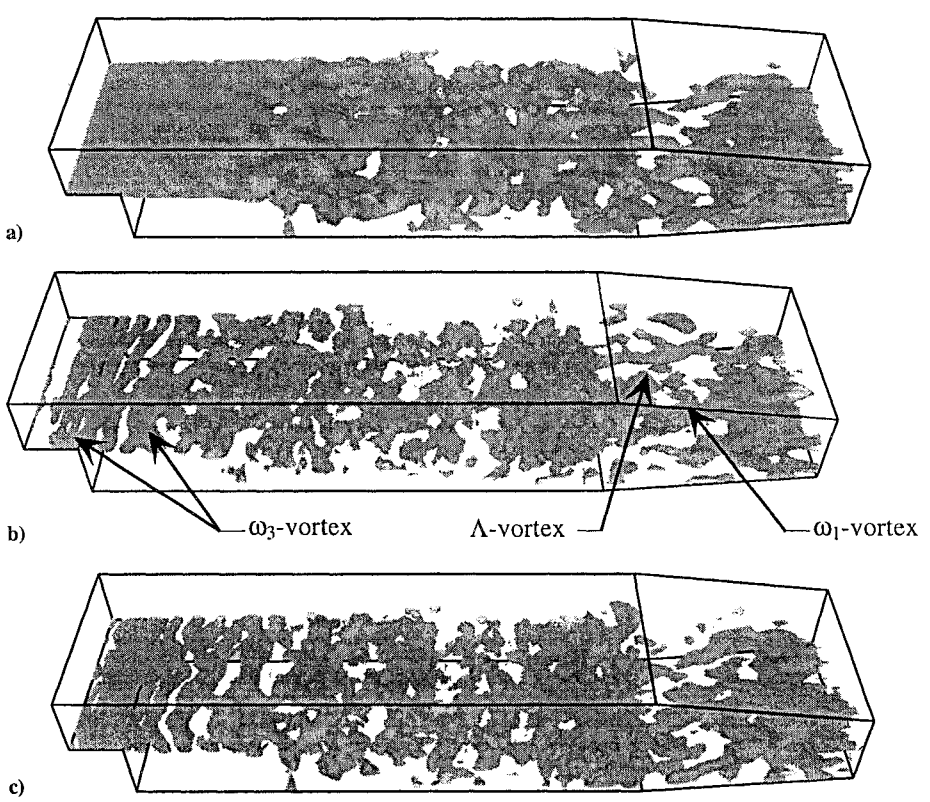

Fig. 9 Perspective view of the flow from the side showing a) isosurface of $|\bar{\omega}| = \frac{3}{2}u_0/h$ from run B1, b) isosurface of $|\bar{\omega}| = \frac{3}{2}u_0/h$ filtered by the Q criterion for run A2, and c) isosurface of $|\bar{\omega}| = \frac{3}{2}u_0/h$ filtered by the Q criterion for run B1.

hence, a mixed pattern of Ω and big Λ vortices are formed, which impinge on the wall and are either carried away downstream and transformed into archlike structures or become trapped in the recirculation bubble.

By comparing instantaneous vorticity distributions between runs B2, B1 (Fig. 8), and B6, using the OEEVM, some additional but anticipated effects of spatial resolution become evident. Although both first- and second-order statistical moments of $\bar{\nu}$ are reasonably well reproduced on all three grids, having a characteristic cell size of 2Δ, $3\Delta/2$, and Δ, respectively, the vorticity dynamics appears only resolved down to scales of $\mathcal{O}(4\Delta)$, $\mathcal{O}(9\Delta/4)$, and $\mathcal{O}(2\Delta)$, respectively. This implies that the small-scale vorticity dynamics appears of secondary importance to the mean flow as long as the SGS model can adequately deplete kinetic energy out of the wavelengths close to the cutoff wavelength λ_c to prevent aliasing. However, as can be observed from Figs. 3 and 4, the statistics, and in particular the second-order statistics, agree increasingly less favorably with measurements for decreasing resolution. Thus, it can be expected that on even coarser grids the results will deteriorate. For this case we presume that the upper resolution limit is $\mathcal{O}(2\Delta)$, due to Reynolds

number and geometrical reasons, i.e., the step height must be adequately resolved. The requirements on the SGS model are more rigorous for coarse grid simulations because the SGS models must be able to correctly emulate even more flow physics. In fact, in the present investigation, runs B2–B5 may be referred to as very LES[33,39] due to the coarse resolution, and hence, it may be argued that the use of more sophisticated SGS models may improve predictions.

VII. Summary and Concluding Remarks

LES and MILES models have been used to examine rearward-facing step flow at Reynolds numbers ranging from $Re = 15 \times 10^3$ to 37×10^3. Three SGS models have been used to close the LES equations and to parameterize effects of the unresolved flow on the resolved flow. Different grids were used to examine the effects of resolution on the first- and second-order statistical moments of $\bar{v}$. For comparison two-dimensional transient simulations using similar grids were performed with conventional RAS models using the well-known k–ε model.

Comparison of first- and second-order statistical moments of $\bar{v}$ for various LES and MILES models with experimental data suggests that these quantities and some key parameters, such as the Strouhal number, the growth rate of the shear layer, and the reattachment length, are practically independent of the SGS model, at least for this flow and for the space–time resolutions used. This further suggests that the predicted energy spectra depend on the effects of the SGS model mainly toward the high wave number end of the inertial range. Similarly, the predicted probability density of vorticity appears largely independent of SGS model for low-intensity vortical structures, whereas for high-intensity structures some differences can be observed. Furthermore, the probability densities of the velocity components exhibit characteristic features related to particular SGS models. In support of other studies,[13,28,39] this corroborates the conjecture that LES is rather insensitive to the SGS model as long as the resolution is fine enough and if the model can correctly channel kinetic energy out of the wave numbers close to the cutoff wave number to prevent aliasing.

Simulations were also performed for other step-height Reynold numbers, corresponding to situations studied experimentally by Pitz and Daily[31] to investigate both the LES model and its predictive capabilities and the flow itself. The LES models were found reasonably accurate and well behaved inasmuch as all trends in the statistical moments of the velocity and the global parameters obtained from experiments could be verified by these simulations. Again, the results are found rather insensitive to the details of the SGS models. The coarse grid LES were capable of accurately reproducing the first-order statistical moments and the global parameters, whereas higher-order statistical moments were less accurately captured, and not surprisingly, the vorticity dynamics appears less well predicted. This implies that the spatial resolution is on the limit of being sufficient for detailed predictions. The simulation data were also used to test a proposed scaling law for the number of grid points and time steps required for a working LES and to generate a database of first- and second-order statistical moments of velocity for rearward-facing step flow at $Re = 15 \times 10^3$, 22×10^3, and 37×10^3, which can be used to examine and calibrate conventional RAS models.

The instantaneous flow was also investigated to gain additional insight into the vorticity dynamics and how the evolution of the vorticity is affected by the SGS models. It is evident that the coherent vortical structures are similar to those of a free shear layer before curvature effects begin to dominate. Primary vortices initiated by Kelvin–Helmholz instabilities are shed off the step and are observed to undergo various pairing and reconnection processes during which the vorticity field loses most of its original coherence. A possible scenario for the vortex dynamics in the rearward-facing step configuration, thus, can be 1) quasi-two-dimensional Kelvin–Helmholz coherent vortices are shed behind the step, 2) they undergo helical-pairing interactions, 3) a mixed pattern of Ω and big Λ vortices are formed, 4) these impinge on the lower wall, and 5) they are either carried away downstream and transformed into archs or become trapped in the recirculation bubble.

Acknowledgments

The author wishes to acknowledge H. G. Weller and G. Tabor for many valuable discussions and for collaboration in developing the multi-purpose computational fluid dynamics code FOAM used in the present study.

References

[1]Wygnanski, I., and Fiedler, H. E., "The Two-Dimensional Mixing Region," *Journal of Fluid Mechanics*, Vol. 41, 1970, pp. 327–361.

[2]Brown, G. L., and Roshko, A., "On Density Effects and Large Structures in Turbulent Mixing Layers," *Journal of Fluid Mechanics*, Vol. 64, 1974, pp. 775–816.

[3]Chandrsuda, C., Mehta, R. D., Weir, A. D., and Bradshaw, P., "Effect of Free-Stream Turbulence on Large Structures in Turbulent Mixing Layers," *Journal of Fluid Mechanics*, Vol. 85, 1978, pp. 693–704.

[4]Eaton, J. K., and Johnston, J. P., "Turbulent Flow Reattachment: An Experimental Study of the Flow and Structure Behind a Backward Facing Step," Stanford Univ., Rept. MD-39, Stanford, CA, 1980.

[5]Silveira-Neto, A., Grand, D., Métais, O., and Lesieur, M., "A Numerical Investigation of the Coherent Vortices in Turbulence Behind a Backward Facing Step," *Journal of Fluid Mechanics*, Vol. 256, 1993, pp. 1–25.

[6]Arnal, M., and Friedrich, R., "Large Eddy Simulation of a Turbulent Flow with Separation," *Turbulent Shear Flows VIII*, Springer–Verlag, Berlin, 1993, p. 169.

[7]Le, H., and Moin, P., "Direct Numerical Simulation of Turbulent Flow over a Backward Facing Step," Stanford Univ., Rept. TF-58, Stanford, CA, 1994.

[8]Lions, P. L., *Mathematical Topics in Fluid Mechanics*, Oxford Science, Oxford, 1996, pp. 1–16.

[9]Speziale, C. G., "Modeling of Turbulent Transport Equations," *Simulation and Modeling of Turbulent Flows*, edited by T. B. Gatski, M. Y. Hussaini, and J. L. Lumeley, Oxford Univ. Press, New York, 1996, pp. 185–242.

[10]Galperin, B., and Orszag, S. A. (eds.), *Large Eddy Simulation of Complex Engineering and Geophysical Flows*, Cambridge Univ. Press, Cambridge, England, UK, 1993.

[11]Rogallo, R. S., and Moin, P., "Numerical Simulation of Turbulent Flows," *Annual Review of Fluid Mechanics*, Vol. 16, 1984, pp. 99–137.

[12]Lesieur, M., and Metais, O., "New Trends in Large Eddy Simulation of Turbulence," *Annual Review of Fluid Mechanics*, Vol. 28, 1996, pp. 45–63.

[13]Boris, J. P., Grinstein, F. F., Oran, E. S., and Kolbe, R. J., "New Insights Into Large Eddy Simulation," *Fluid Dynamics Research*, Vol. 10, 1992, pp. 199–227.

[14]Fureby, C., and Tabor, G., "Mathematical and Physical Constraints on Large Eddy Simulations," *Journal of Theoretical and Computational Fluid Dynamics*, Vol. 9, No. 2, 1997, pp. 85–102.

[15]Ghosal, S., and Moin, P., "The Basic Equations for the Large Eddy Simulation of Turbulent Flows in Complex Geometries," *Journal of Computational Physics*, Vol. 118, 1995, pp. 24–37.

[16]Speziale, C. G., "Galilean Invariance of Sub Grid Scale Stress Models in Large Eddy Simulations of Turbulence," *Journal of Fluid Mechanics*, Vol. 156, 1985, pp. 55–62.

[17]Vreman, B., Geurts, B., and Kuerten, H., "Realizability Conditions for the Turbulent Stress Tensor in Large Eddy Simulation," *Journal of Fluid Mechanics*, Vol. 278, 1994, pp. 351–362.

[18]Yoshizawa, A., "Statistical Theory for Compressible Shear Flows, with the Application to Subgrid Modelling," *Physics of Fluids A*, Vol. 29, No. 7, 1986, pp. 2152–2163.

[19]Germano, M., Piomelli, U., Moin, P., and Cabot, W. H., "A Dynamic Sub Grid Scale Eddy-Viscosity Model," *Physics Fluids A*, Vol. 3, No. 7, 1991, pp. 1760–1765.

[20]Meneveau, C., Lund, T. S., and Cabot, W. H., "A Lagrangian Dynamic Sub Grid Scale Model of Turbulence," *Center of Turbulence Research Annual Research Briefs*, 1994, p. 271.

[21]Fletcher, C. A. J., *Computational Methods in Fluid Dynamics*, Vol. 2, Springer–Verlag, Berlin, 1992, pp. 242–244.

[22]Weller, H. G., Tabor, G., Jasak, H., and Fureby, C., "A Tensorial Approach to CFD Using Object Oriented Techniqes," *Computers in Physics*, Vol. 12, No. 6, 1998, pp. 620–631.

[23]Fureby, C., Tabor, G., Weller, H. G., and Gosman, A. D., "A Comparative Study of Sub Grid Scale Models in Isotropic Homogeneous Turbulence," *Physics of Fluids*, Vol. 9, No. 5, 1997, pp. 1416–1429.

[24]Jimenez, J., Wray, A., Saffman, P., and Rogallo, R., "The Structure of Intense Vorticity in Isotropic Turbulence," *Journal of Fluid Mechanics*, Vol. 255, Oct. 1993, pp. 65–90.

[25]Porter, D. H., Pouquet, A., and Woodward, P. R., "Kolmogorov-Like Spectra in Decaying Three-Dimensional Supersonic Flows," *Physics of Fluids*, Vol. 6, No. 6, 1994, pp. 2133–2144.

[26]Oberman, E. A., and Zabusky, N. J., "Evolution and Merger of Isolated Vortex Structures," *Physics of Fluids*, Vol. 25, No. 8, 1982, pp. 1297–1304.

[27]Grinstein, F. F., "Self-Induced Vortex Ring Dynamics in Subsonic Rectangular Jets," *Physics of Fluids*, Vol. 7, No. 10, 1995, pp. 2519–2521.
[28]Fureby, C., and Grinstein, F. F., "Monotonically Integrated Large Eddy Simulation of Free Shear Flows," *AIAA Journal*, Vol. 37, No. 5, 1999, pp. 544–556; also AIAA Paper 98-0537, Jan. 1998.
[29]Boris, J. P., and Book, D. L., "Flux Corrected Transport I, SHASTA, a Fluid Transport Algorithm that Works," *Journal of Computational Physics*, Vol. 11, 1973, pp. 38–69.
[30]Borue, V., and Orszag, S. A., "Local Energy Flux and Subgrid-Scale Statistics in Three Dimensional Turbulence," *Journal of Fluid Mechanics*, Vol. 366, 1998, pp. 1–31.
[31]Pitz, R. W., and Daily, J. W., "Experimental Study of Combustion: The Turbulent Structure of a Reacting Shear Layer Formed at a Rearward Facing Step," NASA CR 165427, Aug. 1981.
[32]Westphal, R. V., Johnston, J. P., and Eaton, J. K., "Experimental Study of Flow Reattachment in a Single-Sided Sudden Expansion," Stanford Univ., Rept. MD-41, Stanford, CA, 1984.
[33]Woodruff, S. L., Seiner, J. M., and Hussaini, M. Y., "Grid-Size Dependence Considerations for Sub-Grid Scale Models for LES of Kolmogorov Flows," American Physical Society Div. of Fluid Dynamics Meeting, San Francisco, 1997.
[34]Durst, F., and Schmitt, F., "Experimental Studies of High Reynolds Number Backwards-Facing Step Flows," *Proceedings of the Third International Symposium on Turbulent Shear Flows*, 1985, p. 18.1.
[35]Fujii, S., Gomi, M., and Eguchi, K., "A Remote Laser-Probe System for Velocity and Temperature Measurements," *Journal of Fluids Engineering*, Vol. 105, June 1983, pp. 128–136.
[36]Metcalfe, R. W., Orszag, S. A., Brachet, M. E., Menon, S., and Riley, J. J., "Secondary Instability of a Temporally Growing Mixing Layer," *Journal of Fluid Mechanics*, Vol. 184, 1987, pp. 207–218.
[37]Blackburn, H. M., Mansour, N. N., and Cantwell, B. J., "Topology in Fine Scale Motions in Turbulent Channel Flow," *Journal of Fluid Mechanics*, Vol. 310, 1996, pp. 269–292.
[38]Hunt, J. C. R., Wray, A. A., and Moin, P., "Eddies, Stream and Convergence Zones in Turbulent Flows," Center of Turbulence Research, Rept. CTR-S88:193, 1988.
[39]Speziale, C. G., "Turbulence Modeling for Time-Dependent RANS and VLES: A Review," *AIAA Journal*, Vol. 36, No. 2, 1998, pp. 173–184.

K. Kailasanath
Associate Editor